Published in final edited form as:
Biochemistry. 2012 January 31; 51(4): 926–935. doi:10.1021/bi201674d.

Thermodynamics of Coupled Folding in the Interaction of Archaeal RNase P Proteins RPP21 and RPP29

Yiren Xu[a,b,c,1], **Sri Vidya Oruganti**[b,c], **Venkat Gopalan**[a,b,c], and **Mark P. Foster**[a,b,c,*]

[a]Ohio State Biochemistry Program, Center for RNA Biology, The Ohio State University, Columbus, OH 43210, USA

[b]Department of Biochemistry, Center for RNA Biology, The Ohio State University, Columbus, OH 43210, USA

[c]Center for RNA Biology, The Ohio State University, Columbus, OH 43210, USA

Abstract

We have used isothermal titration calorimetry (ITC) to identify and describe binding-coupled equilibria in the interaction between two protein subunits of archaeal ribonuclease P (RNase P). In all three domains of life, RNase P is a ribonucleoprotein complex that is primarily responsible for catalyzing the Mg^{2+}-dependent cleavage of the 5′ leader sequence of precursor tRNAs during tRNA maturation. In archaea, RNase P has been shown to be composed of one catalytic RNA and up to five proteins, four of which associate in the absence of RNA as two functional heterodimers, POP5-RPP30 and RPP21-RPP29. NMR studies of the *Pyrococcus furiosus* RPP21 and RPP29 proteins in their free and complexed states provided evidence for significant protein folding upon binding. ITC experiments were performed over a range of temperatures, ionic strengths, pH values and in buffers with varying ionization potential, and with a folding-deficient RPP21 point mutant. These experiments revealed a negative heat capacity change (ΔC_p), nearly twice that predicted from surface accessibility calculations, a strong salt dependence to the interaction and proton release at neutral pH, but a small net contribution from these to the excess ΔC_p. We considered potential contributions from protein folding and burial of interfacial water molecules based on structural and spectroscopic data. We conclude that binding-coupled protein folding is likely responsible for a significant portion of the excess ΔC_p. These findings provide novel structural-thermodynamic insights into coupled equilibria that enable specificity in macromolecular assemblies.

We have used isothermal titration calorimetry (ITC) to identify and describe the thermodynamics of binding-coupled equilibria in the interaction between two protein subunits of archaeal ribonuclease P (RNase P), a ribonucleoprotein (RNP) complex that is primarily responsible for endonucleolytic removal of the 5′ leader sequence during tRNA maturation (1-3). RNase P was first shown to function as a ribozyme in bacteria, where the mass ratio between the large catalytic RNase P RNA (RPR) and the small protein (RNase P Protein, RPP) is 90:10 (2, 4). In contrast, the RPR in eukaryotes is accompanied by on the order of nine proteins, accounting for 70% of the mass of eukaryal RNase P (2, 5, 6). Archaeal RNase P appears to be an intermediate between bacterial and eukaryal enzymes,

*Corresponding author: 484 West 12th avenue, Columbus, OH 43210, USA. Phone: (614) 292 1377, fax: (614) 292 6773, foster.281@osu.edu.
[1]Present address; Genentech Inc., 1 DNA way, MS 97B, South San Francisco, CA 94080. Phone: (650) 467 6613, yirenxujoy@gmail.com

Supporting Information Supporting Information Available. Tables of thermodynamic data, sequence alignments, representative calorimetric thermograms. This material is available free of charge via the Internet at http://pubs.acs.org.

with 4 to 5 RPPs and a mass ratio of ~50:50 between RNA and proteins (2, 7). Interestingly, the increased RPP content in RNase P is associated a decrease in the pre-tRNA cleavage catalytic activity of the isolated RPR in the three domains of life (2, 8, 9). Thus, comparative studies of these RNase P variants will help address the manner by which protein cofactors might subsume some of the structural and functional responsibilities of the RNA catalyst.

Recent attention has been drawn to archaeal RNase P due to its semblance to the eukaryal enzyme, yet simpler architecture (10). Five distinct proteins have been identified to be associated with the RPR in *Pyrococcus furiosus* (*Pfu*) RNase P, four of which function as two binary complexes (10, 11). POP5-RPP30 has been shown to interact with the catalytic domain (C-domain) of the RPR and enhances the cleavage rate, k_{cat} (12, 13), while RPP21-RPP29 binds to the RPR specificity domain (S-domain) and increases substrate affinity, K_S (12, 14). The fifth protein, L7Ae, is thought to recognize a kink-turn (K-turn) structural motif on the RPR and has been shown to elevate the temperature of optimal activity of the in vitro reconstituted enzyme from 55°C to 70°C (15, 16).

NMR studies of the *Pfu* RPP21 and RPP29 proteins in isolation and in their 30-kDa 1:1 complex showed that several structural elements observed in the complex are poorly formed in the free proteins (14, 17). Structural studies of RPPs from several archea, including *Pfu* and the highly homologous *Pyrococcus horikoshii* (*Pho*), have revealed that RPP21 is a member of the zinc ribbon fold family, with an N-terminal helix-turn-helix (17, 18), while RPP29 is a member of the Sm fold family, consisting of a central beta barrel with helices at both N and C termini (19-21). Both *Pfu* RPP21 and RPP29 are highly basic proteins, with isoelectric points (pI) estimated at 10.3 and 10.2 (http://web.expasy.org/protparam/), as consequence of high proportion of positively charged Lys or Arg residues (RPP21, 30%; RPP29, 20%). The assembled RPP21-RPP29 complex projects an extensive electropositive surface on one side, possibly for complementary electrostatic pairing with the negatively charged surface of the RNA subunit (14). Their protein-protein interface is composed of helices 1-4 and strand β2 of RPP29, and the N-terminal helices of RPP21 (Figure 1, S1), and is characterized by both hydrophobic and electrostatic interactions, leading to surface burial of about 2400 $Å^2$. A large fraction of the region comprising this interface, a total of 50 residues, including residues 17-48 and 116-123 of RPP29 and residues 9-18 of RPP21, are insufficiently structured in the isolated proteins to produce observable NMR signals (due to dynamic exchange between multiple conformations on timescales that lead to signal broadening), but become structured and NMR-observable in the presence of its partner (14, 17).

In this paper, we report the thermodynamic characterization of the *Pfu* RPP21-RPP29 association using isothermal titration calorimetry (ITC). The heat capacity change accompanying complex formation, $\Delta C_{p,obs}$, was measured as a means of assessing the thermodynamic impact of the spectroscopically-observed coupled folding during the specific interaction between the proteins (22). A much larger negative $\Delta C_{p,obs}$ was obtained than that predicted from changes in solvation from the accessible surface area, ΔASA, buried in the interface between the proteins (i.e., the hydrophobic effect). To assess the correlation between this thermodynamic parameter and structural insights related to the extent of coupled folding observed by NMR, we considered other thermodynamic linkages that could contribute to $\Delta C_{p,obs}$ (ion, proton and water), and uncovered important correlations to folding and binding. These insights were corroborated through analysis of a point mutant (RPP21/A14V) that exhibits less coupled folding based on NMR analysis, and a smaller $\Delta C_{p,obs}$. This structure-thermodynamic analysis has yielded important correlations between global thermodynamic measurements and the details of residue-specific interactions that enable assembly of the RPP21-RPP29 complex. These insights may prove to be generally applicable for understanding the assembly of multi-subunit RNP complexes.

Materials and Methods

Structure-Thermodynamic Calculations

The extent and character of the RPP21-RPP29 intermolecular interface was analyzed using the VADAR webserver (http://vadar.wishartlab.com/) (23), with the default parameters for definitions of radii and residue polarity, and method of surface calculation. The coordinates from all ten models of the NMR structure of the *Pfu* RPP21-RPP29 complex (PDB ID: **2KI7**), were used as input to VADAR either intact, or after separating coordinates for the two chains. The mean and standard deviation of intermolecular polar and nonpolar surface burial were obtained by comparing the accessible surface areas of the complex and individual chains. A structurally predicted heat capacity change, $\Delta C_{p,str}$, was computed from the change in accessible polar and nonpolar surface from the empirical relation (24)

$$\Delta C_{p,str} = 0.45\Delta ASA_{np} - 0.26\,\Delta ASA_{polar} \quad (1)$$

where ΔASA_{np} and ΔASA_{polar}, are the changes in surface accessible nonpolar and polar or charged surface areas, respectively.

Sample preparation

The *Pfu* RPP29 and RPP21 proteins were overexpressed and purified as previously described (14, 17, 25). The same purification procedure as for wild type RPP21 was used to obtain purified *Pfu* RPP21/A14V, in which Ala14 is mutated to Val. After dialysis into the NMR buffer individually (10 mM Tris pH 6.7, 10 mM KCl, 0.3 mM $ZnCl_2$, 0.02% NaN_3), each protein solution (< 2 mL) was transferred into a membrane tubing (Spectra/Por 3 dialysis tubing, 3.5K MWCO), and both the proteins were dialyzed twice for ≥ 6 h in the same container against a 250 to 350-fold excess of the standard ITC buffer [20 mM cacodylate (pH 6.7), 10 mM KCl, 0.3 mM $ZnCl_2$, and 0.02% NaN_3) at room temperature. Cacodylate buffer was chosen due to its small ionization heat change from −0.41 kcal mol^{-1} at 10°C to −1.33 kcal mol^{-1} at 55°C, resulting in a relatively temperature-independent pH within the experimental temperature range (26). Protein concentrations were determined from extinction coefficients calculated based on their amino acid sequence (37,470 M^{-1} cm^{-1} for *Pfu* RPP29 and 16,180 M^{-1} cm^{-1} for *Pfu* RPP21) at 280 nm (http://www.expasy.ch/tools/protparam.html). The ITC samples were further diluted to the desired concentrations using the same batch of buffer that was used for dialysis, and were thoroughly degassed under vacuum with gentle stirring before use.

Isothermal titration calorimetry

All ITC experiments were carried out on a VP-ITC calorimeter (MicroCal, Inc., Northhampton, MA) with a first 3 μL injection (discarded during analysis) followed by a series of 5 μL injections with a spacing of at least 400 s between each injection. The measured heat pulses for each injection were integrated and normalized per mole of the injectant to obtain the binding enthalpy, ΔH_{obs}. Heats of dilution were obtained by averaging the last few integrated heat pulses after saturation, and that value was subtracted from all the integrated heat pulses. The corrected ΔH_{obs} were plotted as a function of molar ratio and fit via nonlinear least squares regression to a single binding site model to obtain values of stoichiometry (N) and association constant (K_A). The Gibbs free energy of binding (ΔG_{obs}) and entropy change (ΔS_{obs}) were obtained from the Gibbs relation:

$$\Delta G = -RT\ln K_A = \Delta H - T\Delta S \quad (2)$$

where, R is the gas constant and T is the temperature in Kelvin.

The bulk thermodynamics of the interactions are more completely described with a measurement of the heat capacity change of binding (ΔC_p), which defines the temperature dependence of ΔH and ΔS:

$$\Delta H(T) = \Delta C_p (T - T_H) \quad (3)$$

$$\Delta S(T) = \Delta C_p \ln (T/T_S) \quad (4)$$

where T_H and T_S are the temperatures at which the net binding ΔH and ΔS are zero, respectively. Thus, ΔC_p was obtained from the slope of $\partial\Delta H/\partial T$ in titrations of RPP29 into RPP21 performed over the temperature range of 10°C to 55°C (27). T_S was obtained from the modified Gibbs-Helmholtz relation, which combines equations 2-4 :

$$\Delta G(T) = \Delta C_p (T - T_H) - T\Delta C_p \ln (T/T_S) \quad (5)$$

Likewise, titrations of RPP29WT into RPP21/A14V were performed in standard ITC buffer from 5°C to 55°C, yielding ΔH_{obs}, and subsequently $\Delta C_{p,obs}$.

Ion and proton linkage effect

Protein stock solutions were thoroughly dialyzed twice in the standard ITC buffer containing 50 mM, 100 mM and 150 mM KCl, respectively. A reverse titration of RPP21 into RPP29 was performed due to the low solubility of RPP29 at KCl concentrations above 150 mM. The ion linkage number was obtained from the slope of $\partial(\log K_A)/\partial(\log I)$, where the sign of the slope indicates whether the ions are absorbed (slope > 0) or released (slope < 0) (28). The same set of experiments were performed at 10°C and 55°C in order to measure the effect of ion linkage on the net ΔH_{obs} within the experimental temperatures.

To determine proton linkage, the protein stock solutions were dialyzed twice in buffers with different buffer ionization enthalpies (ΔH_{ion}), namely cacodylate and ACES, at two different pH values, 6.7 and 6.1 (26). As for ion linkage, the dependence of ΔH_{obs} on ΔH_{ion}, $\partial\Delta H_{obs}/\partial\Delta H_{ion}$, reports the number of protons (N_{H+}) that are transferred between the proteins and the buffer, with a positive sign of N_{H+} indicating proton uptake (protonation), and proton release (deprotonation) from a negative dependence. With N_{H+} determined, the net binding enthalpy ΔH_{obs} was corrected, at each temperature, for the enthalpy of ionization to obtain the enthalpy of binding (ΔH_{bind}) (27, 29):

$$\Delta H_{obs} = \Delta H_{bind} + N_{H+} \Delta H_{ion} \quad (6)$$

Correcting ΔH_{obs} at each temperature for the proton linkage effect yielded a corrected ΔC_p for subsequent structure/thermodynamic analysis.

ΔC_p and binding-coupled folding

Structural/thermodynamic relationships have established empirical and theoretical links between the magnitude of ΔC_p and the extent of binding-coupled protein folding (22, 30-32). Following this approach, we used the corrected ΔC_p to obtain a thermodynamic estimate for the number of residues (ℜ) that become ordered upon association of *Pfu* RPP21 and RPP29. Briefly, the approach stipulates that for a protein-protein interaction, at the T_S (the temperature at which ΔS_{assoc} is zero), the entropy changes from the hydrophobic effect (ΔS_{HE}) and losses of rotational and translational degrees of freedom (ΔS_{rt}), are balanced by other effects including binding-induced folding (ΔS_{other}).

$$\Delta S_{assoc}=0=\Delta S_{HE}+\Delta S_{rt}+\Delta S_{other} \quad (7)$$

ΔS_{HE} is well correlated with changes in nonpolar surface area, and can be determined empirically from ΔC_p (after correction for other effects):

$$\Delta S_{HE}=1.35\ \Delta C_p \ln\ (T_S/386) \quad (8)$$

The entropy change from loss of rotational and translation degrees of freedom, ΔS_{rt}, can be derived on statistical thermodynamic grounds to correspond to the cratic entropy of 8 cal mol^{-1} K^{-1} (24, 33), though an empirical value of 50 ± 10 cal mol^{-1} K^{-1} has been found to agree with structural data (22); we used this empirical estimate here. Finally, an empirical analysis of ΔS_{other} from folding of a number of different proteins yielded an average folding entropy cost per residue, $\Delta S_{\Re} = -5.6\ \mathrm{cal\ mol^{-1}K^{-1}}$ (22, 31). Thus, $\Re$ was estimated from:

$$\Re=\frac{\Delta S_{other}}{\Delta S_{\Re}}=\frac{-(\Delta S_{HE}+\Delta S_{rt})}{\Delta S_{\Re}}=\frac{1.35\ \Delta C_p \ln\ (T_S/386)-50}{5.6} \quad (9)$$

NMR spectroscopy

Two dimensional ^1H-^{15}N NMR spectra of [U-^{15}N]- and [U-^{15}N, ^{13}C]-RPP21 and RPP21/A14V were recorded at 55°C on a Bruker DRX600 instrument equipped with a cryogenically cooled triple resonance single-axis gradient probe. Samples were ~ 1 mM, with a slight excess of RPP29, in 10 mM Tris–HCl (pH 6.7), 10 mM KCl, 0.3 mM $ZnCl_2$, and 0.02% (w/v) NaN_3, and were prepared as previously described (14, 25).

Results and Discussion

Structure-Thermodynamic Calculations

A change in surface hydration upon formation of a macromolecular complex is generally understood to be the most significant contributor to heat capacity changes ΔC_p that accompany binding and protein folding (24, 30, 31, 34); thus, in principle this thermodynamic parameter, $\Delta C_{p,str}$, can be predicted once high-resolution structural data is available (22, 24). The interface between *Pfu* RPP21 and RPP29 in the NMR-derived structure of their 1:1 complex (Figure 1) buries 642 ± 64 $Å^2$ of polar accessible surface area (ΔASA_{pol}) and 1772 ± 79 $Å^2$ of nonpolar accessible surface area (ΔASA_{np}). Empirical structure-thermodynamic correlations (equation 1) thus predict binding heat capacity change ($\Delta C_{p,str}$) of −630 ± 69 cal mol^{-1} K^{-1}. This $\Delta C_{p,str}$ value is limited by the assumption of only minor changes in the interface between RPP29 and RPP21, and cannot account for contributions from changes in other linked equilibria, such as binding-coupled folding of the proteins.

The RPP21-RPP29 interaction is characterized by a large negative ΔC_p

Titrations of RPP29 into RPP21 performed over a temperature range from 10°C to 55°C yielded high quality ITC data (Figure 2) that allowed accurate determination of ΔH_{obs} (enthalpy change), K_A (association constant) and N (stoichiometry) of binding (Figure 2, S2, Table 1). The temperature dependence of binding enthalpy, $\partial\Delta H/\partial T$, was linear over the temperature range sampled (Figure 3); this observation permits the simplifying assumption that equilibria contributing strongly to ΔH are not substantially shifted over the temperature range sampled (34, 35), although gradual shifts in many equilibria with small contributions cannot be ruled out (36). Fitting the enthalpy data to equation (3) yielded an experimental value of $\Delta C_{p,obs}$ of −1115 ± 18 cal mol^{-1} K^{-1}, nearly twice that predicted from

intermolecular surface burial alone (above). The data also revealed a T_H of 25.4°C (298.6 ± 0.2 K), below which the RPP21-RPP29 interaction is endothermic and above which it is exothermic (Figure 2, Figure 3). It is worth noting that because the enthalpy of binding is near zero at 25°C, binding between RPP21 and RPP29 is undetectable by ITC near this temperature, a consideration that might easily be overlooked when planning calorimetric experiments.

Despite the strong temperature dependence of ΔH, the binding affinity K_A, and thus ΔG, was relatively insensitive to temperature over the range sampled (−9.0 to −10.4 kcal mol^{-1}) (Figure 3, Table 1). From the temperature dependence of K_A and equations 2 and 5, the temperature at which ΔS was zero, T_S, was 34.6°C (307.8 ± 0.1 K). Below this temperature, binding was favored by a net entropy increase (ΔS > 0), and unfavorable above (ΔS < 0). The analysis also illustrates the curvature in the temperature dependence of ΔG (Figure 3).

These experiments provided access to the parameters T_S and ΔC_p, required for structure-thermodynamic interpretation according to equation 9. However, because other linked equilibria can contribute to $\Delta C_{p,obs}$ (34, 35), we sought to first identify and correct for these effects. In particular, we considered significant contributions to $\Delta C_{p,obs}$ from ion and proton linkage, and burial of interfacial water molecules, which have been described as significant contributors to $\Delta C_{p,obs}$ in other systems (28, 29, 36-41).

RPP21-RPP29 binding is accompanied by ion uptake with a small effect on ΔC_p

Two intermolecular ion pairs have been observed in the RPP21-RPP29 interface from both *Pfu* and *Pho* (14, 42). Glu47 and Asp72 of *Pfu* RPP29 are observed to pair with Arg17 and Arg38 of *Pfu* RPP21 (14), and a similar interface is observed in the *Pho* RPP21-RPP29 complex (42). Based on this observation, it was reasonable to expect an effect on the RPP21-RPP29 interaction from changes in solution ionic strength since favorable electrostatic contacts would be weakened at high salt concentration (43, 44). Despite this expectation, the binding affinity K_A *increased* with increasing ionic strength, *I* (Figure 3, S3, Table S1). The $\partial(\log K_A)/\partial(\log I)$ trend appeared to be nonlinear over the ionic strengths sampled. Although it is beyond the scope of this study to explore in depth the underpinnings for this non-linear ionic strength dependence, similar behavior has been reported phenomenologically before (37), and we surmise it reflects equilibria between binding-incompetent conformations at lower ionic strengths, and competition between protein-protein and protein-solute ion pairing interactions at higher ionic strengths.

At 55°C, 30 mM *I* (i.e., the conditions of the NMR experiments (14)), the slope of $\partial(\log K_A)/\partial(\log I)$ was 3.5, indicating that *uptake* of this many ions, not release, is linked to RPP21-RPP29 binding (Figure 3)(28). At 10°C, a similar ionic strength dependence is observed, with a slope of 3.7 at 30 mM *I*. Notably, the nonlinear dependence of $\partial(\log K_A)/\partial(\log I)$ implies that at higher ionic strength, ion *release* favors protein binding, as predicted from the structurally observed intermolecular ion pair. The non-integral number of absorbed ions may be understood by considering the relatively non-specific interaction between solvent ions and an ensemble of unfolded states for the proteins, in which the screening ions transiently exchange between protein and solvent (45). Unfortunately, sample precipitation at higher ionic strengths prevented sampling a wider range of ionic conditions, and more complete characterization of the effect.

These experiments established thermodynamic linkage between ions and protein binding. The contribution of this linkage effect to $\Delta C_{p,obs}$ were directly assessed from independent measurements of $\partial\Delta H_{obs}/\partial T$ at the ionic strengths of interest. Titrations of RPP21 into RPP29 performed in 150 mM KCl over a temperature range from 10°C to 55°C revealed a slightly larger ΔC_p of −1177 ± 15 cal mol^{-1} K^{-1}, almost within experimental error of those

in 10 mM KCl (Figure 3). Thus, while ion linkage is observed to significantly affect the affinity of the RPP21-RPP29 interaction, we find that over the range of 10 to 150 mM KCl, it does not contribute significantly to $\Delta C_{p,obs}$.

RPP21-RPP29 binding involves net proton release

To assess proton linkage in the RPP21-RPP29 interaction, ΔH_{obs} values were measured from ITC titrations at pH 6.7 in buffers with highly divergent ionization enthalpies: cacodylate (ΔH_{ion} = −1.334 kcal mol^{-1} at 55°C) and ACES (ΔH_{ion} = 6.921 kcal mol^{-1} at 55°C) (Table 2, Fig. S4) (26). These experiments revealed a $\partial\Delta H_{obs}/\partial\Delta H_{ion}$ of −0.7, indicating *release* of protons by the proteins to the bulk solvent as a result of complex formation (Table 2) (27, 29). Considering the non-integer proton linkage number and that the pK_a of the imidazole group of histidine sidechains (which might be involved in coupled folding) is typically between pH 5 to 8 (46, 47), we postulated that lowering the pH should increase the linkage number. To test this premise, we performed analogous ITC experiments in cacodylate and ACES buffers at pH 6.1, which yielded a new linkage number of −1.1. These experiments demonstrate that the binding of RPP21 to RPP29 is accompanied by net deprotonation, and most likely implicate histidine sidechains. Note that the experimentally observed linkage numbers could correspond to ionization at one site, or at multiple sites with similar pK_a values.

We sought a structural explanation for the observed proton linkage. There are six histidine residues in the *Pfu* RPP21-RPP29 complex. Four of them (His60^{RPP29}, His67^{RPP21}, His87^{RPP21} and His97^{RPP21}) are away from the protein-protein interface and are in well-structured regions of the free proteins (14). However, two histidines in RPP29 are in the dimer interface, His34^{RPP29} and His46^{RPP29} (Figure 4); the latter, albeit not universally present, is highly conserved among archaeal RPP29 homologs (14). Moreover, both are in the region of the protein (residues 17-48) that is believed to fold upon binding, based on the absence of backbone resonances from NMR spectra in the absence of RPP21 (14). Without a knowledge of the protonation states of histidine side chains, all histidines were assumed to be protonated at both Nε2 and Nδ1 positions during computational refinement of the solution structure of the *Pfu* RPP21-RPP29 complex (14). Consequently, structure calculations could not yield structures in which a deprotonated imidazole nitrogen could accept a hydrogen bond. However, in the homologous *Pho* RPP21-RPP29 crystal structure (42), these histidines in RPP29 appear to be involved in hydrogen bonding interactions that can only be accommodated by Nδ1-deprotonated, Nε2-protonated imidazole rings, both donating and accepting hydrogen bonds; three of those hydrogen bonds are intramolecular, and one is to a glutamate (Glu21^{RPP21}) sidechain carboxylate in RPP21 that is also conserved between *Pfu* and *Pho* (Figure 4, S6). Thus, deprotonation-dependent hydrogen bonding interactions by one or both of these histidine sidechains are a likely source of the experimentally determined proton linkage.

Having identified proton linkage as a contributor to $\Delta C_{p,obs}$, we proceeded to correct this value using equations 3 and 6 (27, 29). Because the ITC experiments were conducted in cacodylate buffer, which has a low ΔH_{ion} (−0.717 kcal mol^{-1} at 25°C) (Table 2), and small temperature dependence (−20.55 cal mol^{-1} K^{-1}) (26), linkage of a single proton required minimal correction of ΔC_p to −1100 ± 18 cal mol^{-1} K^{-1}. This analysis leaves an excess ΔC_p of ~500 cal mol^{-1} K^{-1} ($\Delta C_{p,obs} - \Delta C_{p,str}$) yet unaccounted for by ion and proton binding.

Burial of structured water

The burial of water molecules in a molecular interface has been argued on experimental and theoretical grounds to be a significant source for $\Delta C_{p,obs}$ in interactions involving proteins (36, 39-41). Literature estimates of the contribution to ΔC_p from burying a water molecule

(i.e., transferring from the solvent to the protein) vary widely, from nearly negligible to that of the heat capacity of water of 18 cal mol^{-1} K^{-1} (48), or to as much as 72 cal mol^{-1} K^{-1} for a completely buried water molecule making four hydrogen bonds (36). Based on these approximations, for the excess ΔC_p of ~500 kcal mol^{-1} K^{-1} to be contributed by binding water, on the order of 7-28 water molecules would have to be fully sequestered upon formation of the RPP21-RPP29 complex.

To indirectly assess whether significant numbers of water molecules might become sequestered in the interface upon binding, we examined ordered water molecules in the 2.2 Å crystal structure of the highly homologous *Pho* RPP21-RPP29 complex (2ZAE)(Figure S6)(42). In this structure, there are two copies of the RPP21-RPP29 complex in the asymmetric unit, providing additional confidence in the identification of structured waters. Well-defined density within a cavity inside RPP29 has been assigned to a water molecule modeled within hydrogen bonding distance of the carboxylate sidechains of Glu47 and Glu73, and the backbone amides of Leu48 and Ile49. Though not in direct intramolecular contact with other residues, $Glu47^{RPP29}$ is positioned to form an intermolecular ion pair with the guanidinium group of $Arg17^{RPP21}$ (Arg22 in *Pho*; Figure S6). Moreover, $Glu47^{RPP29}$ and $Leu48^{RPP29}$ are in a poorly structured region in the free *Pfu* protein. Consequently, if coupled folding of RPP29 involves sequestration of the crystallographically observed water molecule, this too could contribute to $\Delta C_{p,obs}$. Although this premise is difficult to confirm experimentally (39), if we assume that four new hydrogen bonds are formed upon binding-coupled folding, this could contribute as much as 72 cal mol^{-1} K^{-1} to $\Delta C_{p,obs}$ (36). Additional ordered water molecules were observed in the *Pho* RPP21-RPP29 complex, 23 of which are within 1 Å of an asymmetry-related water molecule. However, these are either mostly surface exposed or far from the protein-protein interface, and therefore would not be expected to contribute significantly to binding $\Delta C_{p,obs}$, unless their ordering accompanies the binding-coupled folding of those regions of the protein with which they interact. Because such changes in protein solvation would be included in the empirically determined parameter $\Delta S_{\Re}$(22), we do consider them explicitly here. If only a single buried interfacial water molecule is taken as a contributor to $\Delta C_{p,obs}$, this value can be corrected from −1100 to −1028 cal mol^{-1} K^{-1}.

Extent of coupled folding from ITC agrees with NMR data

Application of equation 9 to the experimentally determined T_S (308 K) and corrected ΔC_p (−1028 cal mol^{-1} K^{-1}) of the *Pfu* RPP21-RPP29 interaction yields an $\Re$ of 47, providing a numerical estimate for the effective number of residues that fold upon binding. This number agrees favorably with NMR-observed folding of 50 residues upon formation of the *Pfu* RPP21-RPP29 complex, despite the different metrics involved in the two techniques (Figure 1; residues 17-48 and 116-123 of RPP29 and Residues 9-18 of RPP21) (14). In the NMR studies, “foldedness” was assessed based on the observation and assignment of resonances in standard triple resonance NMR experiments. Since residues in regions of the protein that are meta-stable are subject to conformational sampling on timescales that lead to loss of NMR signals (49), the absence of signals from such regions is often interpreted as indicative of poorly formed structure. Population of such alternative conformations directly leads to an increase in C_p, compared to a protein with a single stable conformation (30, 34, 35), but also through the reorganization of solvent molecules and ions that facilitate folding. Thus, in the case of binding-coupled folding, the large excess negative ΔC_p arises from narrowing of the energy landscape through reduction in the number of conformations that can be significantly populated by the protein and its tightly associated ligands (including ions and water molecules).

This explanation for the magnitude of ΔC_p was corroborated by NMR and ITC studies of a point mutant that interferes with proper formation of the RPP21-RPP29 interface. NMR studies of the interaction between RPP29 and a variant of RPP21 with an Ala-Val substitution at position 14 (RPP21/A14V), revealed a similar extent of binding-coupled protein folding in RPP29, but not in RPP21/A14V. That is, 40 residues from RPP29 (17-48 and 116-123) that did not produce NMR signals in the free protein were observed in the accompanying complex with RPP21/A14V. However, residues 9-18 which give rise to observable signals in the wild type complex (Figure 1), cannot be assigned in the complex of RPP21/A14V with RPP29 (14, 17, 50). Moreover, because Ala14 is in the region of RPP21 that is unstructured in the absence of RPP29 (Figure 1) but makes important intermolecular packing interactions in the complex, this mutation can be expected to affect RPP29 binding more than the integrity of the RPP21 structure. Indeed, ^{1}H-^{15}N NMR spectra of RPP21 and RPP21/A14V are more similar than the corresponding spectra of their complexes with RPP29 (Figure 5); nevertheless, the differences in spectra of the free proteins does indicate that in the free protein Val14 does measurably perturb the RPP21 structure, indicating that this region of the free protein is not fully unfolded. We determined ΔC_p for this interaction via ITC, by measuring ΔH_{obs} of binding from 5°C to 55°C, yielding a $\Delta C_{p,obs}$ of −932 cal mol^{-1} K^{-1}. This value was corrected by assuming, as for the wild-type interaction, 1) insignificant contribution from ion binding to ΔC_p, 2) 0.7 proton transfer upon binding at pH 6.7, and 3) sequestration of one water molecule at a cost of 72 cal mol^{-1} K^{-1}. This yielded a ΔC_p of −845 cal mol^{-1} K^{-1} and a T_S of 304 K for the *Pfu* RPP29WT-RPP21/A14V interaction (Figure 6, S5 and Table S3). Application of equation 9 to these values estimates an $\Re$ of 40 residues folding upon binding. This result is qualitatively consistent with the reduced extent of binding-coupled protein folding evident from the NMR spectra for the interaction of the RPP21/A14V point mutant with RPP29 (40 for the mutant, 50 for the wild type proteins).

Caveats and sources of uncertainty

Structural interpretation of thermodynamic data (22, 24) is complicated by the many interactions that contribute to the net thermodynamic parameters measured, and imprecise knowledge of the magnitude of the effects. As noted above, changes in protein solvation are generally considered to be the major contributor to negative ΔC_P of binding, via the hydrophobic effect (30, 31, 34, 51), though estimates differ on the empirical relation between surface area burial and ΔC_p (24, 51). Moreover, binding-induced heat capacity changes in excess of $\Delta C_{p,str}$ are common in protein-ligand, protein-DNA and protein-protein interactions, even in systems with little evidence for coupled conformational changes (32, 39, 52), complicating efforts to obtain insightful structure-thermodynamic correlations. Similarly, the contribution to ΔC_p from the complete or partial burial of water molecules upon formation of a protein-protein complex is difficult to estimate accurately, and it seems likely that its magnitude will be highly system-dependent. Lastly, estimates of $\Re$, the number of residues that fold upon binding, are further dependent on $\Delta S_{\Re}$, an empirical estimate of the per-residue entropy change that accompanies folding (22, 31); though not explicitly considered in the development of that parameter, it seems likely that $\Delta S_{\Re}$ includes contributions from multiple coupled equilibria, including coupled binding of water molecules, ions and changes in ionization.

Thus, the quantitative insights from the present studies are tempered by a number of sources of uncertainty, if of unequal scope and magnitude: (1) the accuracy in obtaining the relevant calorimetric data ΔH_{obs}, ΔC_p, T_S and K_A, (2) the imperfect empirical relationships between ΔC_p and ΔS_{HE}, and in estimation of $\Delta S_{\Re}$, (3) the magnitude of the effect of binding-coupled water sequestration on $\Delta C_{p,obs}$, and (4) the imperfect correlation between the NMR spectroscopic metric of “foldedness” and the thermodynamic parameters measured. Despite

these limitations, by integrating complementary spectroscopic, crystallographic and mutagenesis data we are able to provide significant qualitative, if not highly quantitative, structure-thermodynamic insights into the interaction between these protein components of archaeal RNAse P.

Conclusion

We have used ITC to gain insights into the disorder to structure transition that accompanies formation of the heterodimer comprising *Pfu* RPP21 and RPP29, two subunits of archaeal RNase P. Titrations uncovered a large negative excess ΔC_p that could not be accounted for by ion or proton linkage, or sequestration of interfacial water molecules, thereby establishing strong thermodynamic linkage of protein folding to binding; the magnitude of this effect is consistent with that expected from qualitative NMR studies. Ion linkage experiments revealed unexpected ion uptake at low ionic strength, suggesting that electrostatic repulsion disfavors formation of favorable intraand intermolecular interactions that otherwise stabilize the complex while proton linkage measurements suggest that histidine side chain deprotonation is required for proper folding and binding. These data provide both global and site-specific insights into the structural and thermodynamic basis for the specific interaction between these highly charged and thermostable proteins, which subsequently assemble with a large RNase P RNA subunit to facilitate tRNA 5′ maturation.

The binding-coupled folding of *Pfu* RPP21 and RPP29 exemplifies the notion that intermolecular interactions are required for formation of functionally relevant structures. Such induced fit, and its implied conformational sampling, lowers the energy barrier for generating complementary macromolecular interfaces and acts as a gating mechanism that enables biological function only upon completion of an array of conformational switches (22, 53-56). Indeed, the unique structural features resulting from coupled folding during assembly of *Pfu* RPP21-RPP29 are likely critical for generating its high-affinity, RNA-binding surface. Although the dramatic changes observed during formation of the *Pfu* RPP21-RPP29 heterodimer are not mirrored in the *Pfu* POP5-RPPP30 complex (57, 58), we recently demonstrated induced-fit during assembly of the archaeal RNase P holoenzyme, wherein the *Pfu* RNase P RNA could rescue *in vitro* a 24-amino acid deletion in RPP29 that compromised its ability to bind RPP21 (59). Therefore, it appears that co-folding of interacting pairs in large RNPs represents a general theme for achieving the specificity and functional payoffs from induced-fit mechanisms.

Supplementary Material

Refer to Web version on PubMed Central for supplementary material.

Acknowledgments

We thank I. R. Kleckner and E. Ihms for helpful discussions.

Funding: This work was supported by grant from the National Institutes of Health to M.P.F and V.G. (GM067807), and from the National Science Foundation to V.G. (MCB 0843543); funds for the ITC200 microcalorimeter were provided by an NIH ARRA supplement to R01 GM063615 to T. M. Henkin and MPF.

Abbreviations

RNase P	ribonuclease P
RNP	ribonucleoprotein

RPR	RNase P RNA
RPP	RNase P protein
Pfu	Pyrococcus furiosus
Pho	Pyrococcus horikoshii
ASA	accessible surface area

References

1. Altman S. A view of RNase P. Mol Biosyst. 2007; 3:604–607. [PubMed: 17700860]
2. Jarrous N, Gopalan V. Archaeal/Eukaryal RNase P: subunits, functions and RNA diversification. Nucleic Acids Res.
3. Smith D, Pace NR. Multiple magnesium ions in the ribonuclease P reaction mechanism. Biochemistry. 1993; 32:5273–5281. [PubMed: 8499432]
4. Guerrier-Takada C, Gardiner K, Marsh T, Pace N, Altman S. The RNA moiety of ribonuclease P is the catalytic subunit of the enzyme. Cell. 1983; 35:849–857. [PubMed: 6197186]
5. Chamberlain JR, Lee Y, Lane WS, Engelke DR. Purification and characterization of the nuclear RNase P holoenzyme complex reveals extensive subunit overlap with RNase MRP. Genes Dev. 1998; 12:1678–1690. [PubMed: 9620854]
6. Kikovska E, Svard SG, Kirsebom LA. Eukaryotic RNase P RNA mediates cleavage in the absence of protein. Proc Natl Acad Sci U S A. 2007; 104:2062–2067. [PubMed: 17284611]
7. Pannucci JA, Haas ES, Hall TA, Harris JK, Brown JW. RNase P RNAs from some Archaea are catalytically active. Proc Natl Acad Sci U S A. 1999; 96:7803–7808. [PubMed: 10393902]
8. Gopalan V. Uniformity amid diversity in RNase P. Proc Natl Acad Sci U S A. 2007; 104:2031–2032. [PubMed: 17287341]
9. Hartmann E, Hartmann RK. The enigma of ribonuclease P evolution. Trends Genet. 2003; 19:561–569. [PubMed: 14550630]
10. Hall TA, Brown JW. Archaeal RNase P has multiple protein subunits homologous to eukaryotic nuclear RNase P proteins. RNA. 2002; 8:296–306. [PubMed: 12003490]
11. Tsai HY, Pulukkunat DK, Woznick WK, Gopalan V. Functional reconstitution and characterization of Pyrococcus furiosus RNase P. Proc Natl Acad Sci U S A. 2006; 103:16147–16152. [PubMed: 17053064]
12. Chen WY, Pulukkunat DK, Cho IM, Tsai HY, Gopalan V. Dissecting functional cooperation among protein subunits in archaeal RNase P, a catalytic ribonucleoprotein complex. Nucleic Acids Res.
13. Pulukkunat DK, Gopalan V. Studies on Methanocaldococcus jannaschii RNase P reveal insights into the roles of RNA and protein cofactors in RNase P catalysis. Nucleic Acids Res. 2008; 36:4172–4180. [PubMed: 18558617]
14. Xu Y, Amero CD, Pulukkunat DK, Gopalan V, Foster MP. Solution structure of an archaeal RNase P binary protein complex: formation of the 30-kDa complex between Pyrococcus furiosus RPP21 and RPP29 is accompanied by coupled protein folding and highlights critical features for protein-protein and protein-RNA interactions. J Mol Biol. 2009; 393:1043–1055. [PubMed: 19733182]
15. Cho IM, Lai LB, Susanti D, Mukhopadhyay B, Gopalan V. Ribosomal protein L7Ae is a subunit of archaeal RNase P. Proc Natl Acad Sci U S A. 107:14573–14578. [PubMed: 20675586]
16. Fukuhara H, Kifusa M, Watanabe M, Terada A, Honda T, Numata T, Kakuta Y, Kimura M. A fifth protein subunit Ph1496p elevates the optimum temperature for the ribonuclease P activity from Pyrococcus horikoshii OT3. Biochem Biophys Res Commun. 2006; 343:956–964. [PubMed: 16574071]
17. Amero CD, Boomershine WP, Xu Y, Foster M. Solution structure of Pyrococcus furiosus RPP21, a component of the archaeal RNase P holoenzyme, and interactions with its RPP29 protein partner. Biochemistry. 2008; 47:11704–11710. [PubMed: 18922021]

18. Kakuta Y, Ishimatsu I, Numata T, Kimura K, Yao M, Tanaka I, Kimura M. Crystal structure of a ribonuclease P protein Ph1601p from Pyrococcus horikoshii OT3: an archaeal homologue of human nuclear ribonuclease P protein Rpp21. Biochemistry. 2005; 44:12086–12093. [PubMed: 16142906]
19. Boomershine WP, McElroy CA, Tsai HY, Wilson RC, Gopalan V, Foster MP. Structure of Mth11/Mth Rpp29, an essential protein subunit of archaeal and eukaryotic RNase P. Proc Natl Acad Sci U S A. 2003; 100:15398–15403. [PubMed: 14673079]
20. Numata T, Ishimatsu I, Kakuta Y, Tanaka I, Kimura M. Crystal structure of archaeal ribonuclease P protein Ph1771p from Pyrococcus horikoshii OT3: an archaeal homolog of eukaryotic ribonuclease P protein Rpp29. RNA. 2004; 10:1423–1432. [PubMed: 15317976]
21. Sidote DJ, Heideker J, Hoffman DW. Crystal structure of archaeal ribonuclease P protein aRpp29 from Archaeoglobus fulgidus. Biochemistry. 2004; 43:14128–14138. [PubMed: 15518563]
22. Spolar RS, Record MT Jr. Coupling of local folding to site-specific binding of proteins to DNA. Science. 1994; 263:777–784. [PubMed: 8303294]
23. Willard L, Ranjan A, Zhang H, Monzavi H, Boyko RF, Sykes BD, Wishart DS. VADAR: a web server for quantitative evaluation of protein structure quality. Nucleic Acids Res. 2003; 31:3316–3319. [PubMed: 12824316]
24. Lavigne P, Bagu JR, Boyko R, Willard L, Holmes CF, Sykes BD. Structure-based thermodynamic analysis of the dissociation of protein phosphatase-1 catalytic subunit and microcystin-LR docked complexes. Protein Sci. 2000; 9:252–264. [PubMed: 10716177]
25. Xu, Y. Department of Biochemistry. Ohio State University; Columbus, Ohio: 2010. Structure and interactions of archaeal RNase P proteins RPP29 and RPP21; p. 254
26. Goldberg RY, et al. Thermodynamic Quantities for the Ionization Reactions of Buffers. J. Phys. Chem. Ref. Data. 2002; 31:231–370.
27. Jelesarov I, Bosshard HR. Isothermal titration calorimetry and differential scanning calorimetry as complementary tools to investigate the energetics of biomolecular recognition. J Mol Recognit. 1999; 12:3–18. [PubMed: 10398392]
28. Lohman TM, Overman LB, Ferrari ME, Kozlov AG. A highly salt-dependent enthalpy change for Escherichia coli SSB protein-nucleic acid binding due to ion-protein interactions. Biochemistry. 1996; 35:5272–5279. [PubMed: 8611514]
29. Baker BM, Murphy KP. Evaluation of linked protonation effects in protein binding reactions using isothermal titration calorimetry. Biophys J. 1996; 71:2049–2055. [PubMed: 8889179]
30. Sturtevant JM. Heat capacity and entropy changes in processes involving proteins. Proc Natl Acad Sci U S A. 1977; 74:2236–2240. [PubMed: 196283]
31. Baldwin RL. Temperature dependence of the hydrophobic interaction in protein folding. Proc Natl Acad Sci U S A. 1986; 83:8069–8072. [PubMed: 3464944]
32. Spolar RS, Livingstone JR, Record MT Jr. Use of liquid hydrocarbon and amide transfer data to estimate contributions to thermodynamic functions of protein folding from the removal of nonpolar and polar surface from water. Biochemistry. 1992; 31:3947–3955. [PubMed: 1567847]
33. Kauzmann W. Some factors in the interpretation of protein denaturation. Adv Protein Chem. 1959; 14:1–63. [PubMed: 14404936]
34. Prabhu NV, Sharp KA. Heat capacity in proteins. Annu Rev Phys Chem. 2005; 56:521–548. [PubMed: 15796710]
35. Eftink MR, Anusiem AC, Biltonen RL. Enthalpy-entropy compensation and heat capacity changes for protein-ligand interactions: general thermodynamic models and data for the binding of nucleotides to ribonuclease A. Biochemistry. 1983; 22:3884–3896. [PubMed: 6615806]
36. Cooper A. Heat capacity effects in protein folding and ligand binding: a re-evaluation of the role of water in biomolecular thermodynamics. Biophys Chem. 2005; 115:89–97. [PubMed: 15752588]
37. Kozlov AG, Lohman TM. Calorimetric studies of E. coli SSB protein-single-stranded DNA interactions. Effects of monovalent salts on binding enthalpy. J Mol Biol. 1998; 278:999–1014. [PubMed: 9600857]
38. Kozlov AG, Lohman TM. Large contributions of coupled protonation equilibria to the observed enthalpy and heat capacity changes for ssDNA binding to Escherichia coli SSB protein. Proteins. 2000; (Suppl 4):8–22. [PubMed: 11013397]

39. Bergqvist S, Williams MA, O'Brien R, Ladbury JE. Heat capacity effects of water molecules and ions at a protein-DNA interface. J Mol Biol. 2004; 336:829–842. [PubMed: 15095863]
40. Morton CJ, Ladbury JE. Water-mediated protein-DNA interactions: the relationship of thermodynamics to structural detail. Protein Sci. 1996; 5:2115–2118. [PubMed: 8897612]
41. Ladbury JE, Wright JG, Sturtevant JM, Sigler PB. A thermodynamic study of the trp repressor-operator interaction. J Mol Biol. 1994; 238:669–681. [PubMed: 8182742]
42. Honda T, Kakuta Y, Kimura K, Saho J, Kimura M. Structure of an archaeal homolog of the human protein complex Rpp21-Rpp29 that is a key core component for the assembly of active ribonuclease P. J Mol Biol. 2008; 384:652–662. [PubMed: 18929577]
43. Record MT Jr. Lohman ML, De Haseth P. Ion effects on ligand-nucleic acid interactions. J Mol Biol. 1976; 107:145–158. [PubMed: 1003464]
44. Record MT Jr. Anderson CF, Lohman TM. Thermodynamic analysis of ion effects on the binding and conformational equilibria of proteins and nucleic acids: the roles of ion association or release, screening, and ion effects on water activity. Q Rev Biophys. 1978; 11:103–178. [PubMed: 353875]
45. Bergqvist S, Williams MA, O'Brien R, Ladbury JE. Reversal of halophilicity in a protein-DNA interaction by limited mutation strategy. Structure. 2002; 10:629–637. [PubMed: 12015146]
46. Markley JL, Finkenstadt WR. Correlation proton magnetic resonance studies at 250 MHz of bovine pancreatic ribonuclease. III. Mutual electrostatic interaction between histidine residues 12 and 119. Biochemistry. 1975; 14:3562–3566. [PubMed: 240383]
47. Edgcomb SP, Murphy KP. Variability in the pKa of histidine side-chains correlates with burial within proteins. Proteins. 2002; 49:1–6. [PubMed: 12211010]
48. Dunitz J. The Entropic Cost of Bound Water in Crystals and Biomolecules. Science. 1994; 264:670. [PubMed: 17737951]
49. Kleckner IR, Foster MP. An introduction to NMR-based approaches for measuring protein dynamics. Biochim Biophys Acta. 2011; 1814:942–968. [PubMed: 21059410]
50. Xu, Y. Ph.D thesis. The Ohio State University; Columbus, OH: 2010.
51. Murphy KP, Privalov PL, Gill SJ. Common features of protein unfolding and dissolution of hydrophobic compounds. Science. 1990; 247:559–561. [PubMed: 2300815]
52. Olsson TS, Ladbury JE, Pitt WR, Williams MA. Extent of enthalpy-entropy compensation in protein-ligand interactions. Protein Sci. 2011; 20:1607–1618. [PubMed: 21739503]
53. Leulliot N, Varani G. Current topics in RNA-protein recognition: control of specificity and biological function through induced fit and conformational capture. Biochemistry. 2001; 40:7947–7956. [PubMed: 11434763]
54. Williamson JR. Induced fit in RNA-protein recognition. Nat Struct Biol. 2000; 7:834–837. [PubMed: 11017187]
55. Schroeder R, Barta A, Semrad K. Strategies for RNA folding and assembly. Nat Rev Mol Cell Biol. 2004; 5:908–919. [PubMed: 15520810]
56. Williamson JR. Cooperativity in macromolecular assembly. Nat Chem Biol. 2008; 4:458–465. [PubMed: 18641626]
57. Kawano S, Nakashima T, Kakuta Y, Tanaka I, Kimura M. Crystal structure of protein Ph1481p in complex with protein Ph1877p of archaeal RNase P from Pyrococcus horikoshii OT3: implication of dimer formation of the holoenzyme. J Mol Biol. 2006; 357:583–591. [PubMed: 16430919]
58. Crowe BL, Bohlen CJ, Wilson RC, Gopalan V, Foster MP. Assembly of the Complex between Archaeal RNase P Proteins RPP30 and Pop5. Archaea. 2011 In Press.
59. Chen WY, Xu Y, Cho IM, Oruganti SV, Foster MP, Gopalan V. Cooperative RNP Assembly: Complementary Rescue of Structural Defects by Protein and RNA Subunits of Archaeal RNase P. J Mol Biol. 2011; 411:368–383. [PubMed: 21683084]

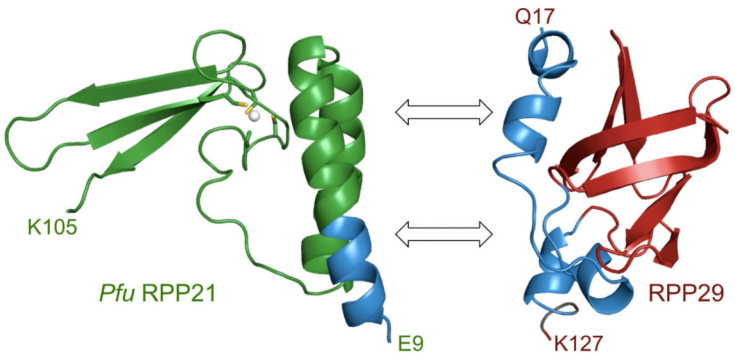

Figure 1.

Structures of *Pfu* RPP21 and RPP29 as observed in their complex.(14, 17) The proteins adopt folds commonly observed in RNA-binding proteins: RPP21 is a zinc ribbon, while RPP29 is a member of the Sm-like proteins. Ribbon diagrams are colored to indicate the structured cores of RPP21 (green) and RPP29 (red) based on NMR studies, with the segments that become ordered upon binding highlighted in blue. For RPP21, zinc-chelating cysteines are shown as sticks, and zinc as a sphere.

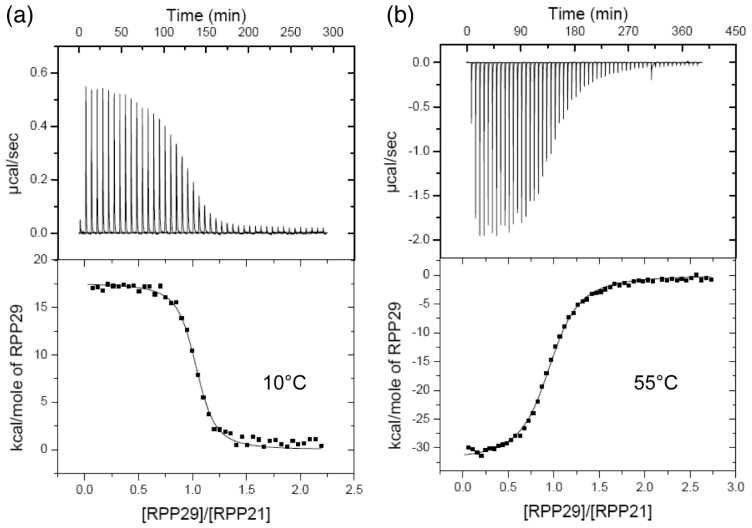

Figure 2.

Calorimetric titration of RPP29 to RPP21 is endothermic at 10°C (a) and exothermic at 55°C (b) in standard ITC buffer (20 mM cacodylate pH 6.7, 10 mM KCl, 0.3 mM $ZnCl_2$ and 0.02% NaN_3). Each peak (top panel) shows the power required to maintain a fixed temperature difference to the reference cell upon injection of 5 μL of 200 μM of RPP29 into 20 μM of RPP21. The integrated heats were normalized per mole of the ligand (RPP29), corrected for heat of dilution and fit to a single binding site model by nonlinear least-squares analysis (bottom panel). Best fit values are shown in Table 1.

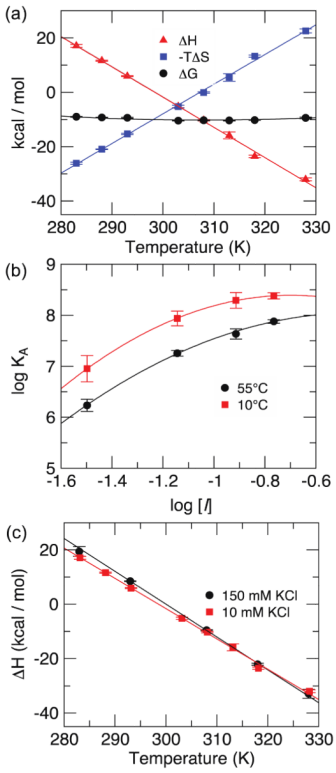

Figure 3.

Thermodynamics of the RPP29-RPP21 interaction as measured by ITC. (a) Temperature dependence of ΔH (red triangles), −TΔS (blue squares) and ΔG = −RT ln K_A (black circles), obtained from fitting the calorimetric data to a one-site binding model. The line for ΔH is a linear fit of the data to equation 3, yielding a slope, ΔC_p of −1115 cal mol^{-1} K^{-1} and x-intercept, T_H of 298.6 K. The line for ΔG shows its curvature and represents the fit of the data to modified Gibbs-Helmholtz relation (equation 5), which reports a T_S of 307.8 K, using the ΔC_p value obtained from the slope of ∂ΔH/∂T. The line through −TΔS was generated from equation 4 using the best-fit values from ∂ΔH/∂T and ∂ΔG/∂T. Uncertainty in plotted thermodynamic values represent the standard deviation of three measurements repeated under the same conditions, except for 20°C (single) and 30°C (duplicate). (b) Ion linkage as assessed by the effect of ionic strength on the calorimetrically determined K_A. Lines represent a phenomenological fit of the data to a quadratic of the form ax^2 +bx + c. The slopes of the log K_A vs. log *I* relationship at 55°C (black) and 10°C (red) are positive at low ionic strength (~3.5 at 30 mM), indicating ion uptake upon binding; negative slopes are implied at higher *I* but could not be measured due to sample precipitation at higher salt concentrations. (c) Temperature dependence of ΔH at two different salt concentrations, 10 and 150 mM KCl. Best fit values at 150 mM KCl are within error of those in 10 mM KCl.

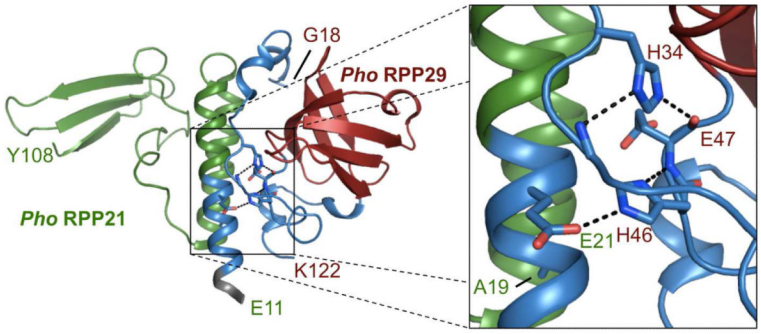

Figure 4.

Hydrogen bonds to histidine side chains in the crystal structure of the *Pho* RPP21-RPP29 complex (PDB ID: **2ZAE**) provides a structural explanation for proton linkage in the binding of *Pfu* RPP21 and RPP29. (a) Cartoon diagram of the *Pho* RPP21-RPP29 complex colored as in Figure 1. The squared region in (a) is magnified in (b), showing the four possible hydrogen bonds. Three of them are intramolecular hydrogen bonds in RPP29 between acceptor E47O and protonated donor H34Nε2, donor G36N and deprotonated acceptor H34Nδ1, and deprotonated acceptor H46Nδ1 and donor E47N within RPP29. One intermolecular hydrogen bond was also observed between acceptor RPP21E21Oε2 and protonated donor RPP29H46Nε2. The residue numbers are labeled in green for RPP21 and in red for RPP29, respectively.

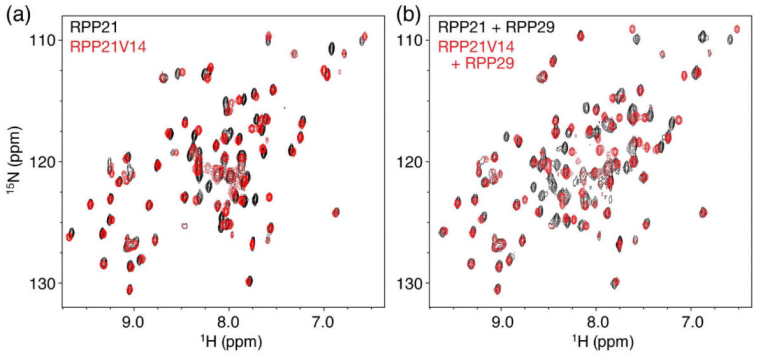

Figure 5.

Two dimensional ^{1}H-^{15}N NMR spectra of RPP21 and RPP21/A14V free and bound to RPP29 reveal differing extent of coupled folding. (a) Overlay of portions of the correlation spectra of RPP21 (black) and RPP21/A14V (red) in their free states, and (b) in the presence of RPP29.

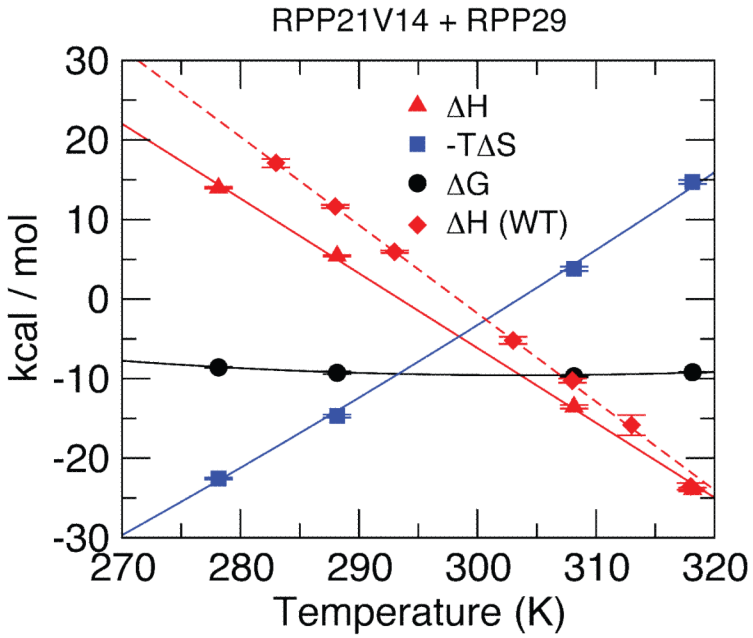

Figure 6.

Temperature dependence of thermodynamic parameters for the interaction of *Pfu* RPP21A1V4 with RPP29. Legends as in Figure 3(a); the ΔH for the wild type (WT) proteins is also included for comparison (red diamonds, dashed line). A ΔC_p (−932 cal mol^{-1} K^{-1}) was obtained by fitting the ΔH data to eq. 3, and T_s (304 K), from equation 5. The smaller negative ΔC_p (i.e., less steep slope) is consistent with less coupled folding for the mutant than for the wild type protein.

Table 1

Temperature dependent thermodynamics for titration of RPP29 into RPP21[a]

Temp	N	K_A (/10^6)	ΔG	ΔH	TΔS
10° C	0.956 ± 0.063	9.17 ± 2.36	−9.00 ± 0.14	17.10 ± 0.53	26.08 ± 0.4
15° C	1.015 ± 0.068	10.91 ± 1.98	−9.26 ± 0.1	11.64 ± 0.21	20.90 ± 0.12
20° C[b]	0.900 ± 0.014	9.55 ± 3.48	−9.35 ± 0.21	5.95 ± 0.15	15.29 ± 0.26
30° C[c]	0.986 ± 0.063	33.15 ± 4.46	−10.42 ± 0.08	−5.19 ± 0.45	5.24 ± 0.51
35° C	0.998 ± 0.101	20.10 ± 2.59	−10.28 ± 0.08	−10.25 ± 0.25	0.05 ± 0.27
40° C	1.030 ± 0.02	17.10 ± 4.17	−10.34 ± 0.14	−15.84 ± 1.27	−5.49 ± 1.39
45° C	1.002 ± 0.062	10.66 ± 0.88	−10.22 ± 0.05	−23.53 ± 0.42	−13.29 ± 0.39
55° C	0.970 ± 0.033	2.04 ± 0.95	−9.40 ± 0.32	−31.98 ± 0.51	−22.56 ± 0.73

[a]Buffer: 20 mM cacodylate (pH 6.7), 10 mM KCl, 0.3 mM $ZnCl_2$, and 0.02% NaN_3. Binding parameters are N (number of RPP29 binding per RPP21), K_A (association equilibrium constant) in M^{-1}, and ΔG, ΔH and TΔS in kcal mol^{-1}. Reported uncertainties are the standard deviation of the three repeat data sets at each temperature, except at 20°C, which are standard fitting errors. Least squares fitting of ΔH and ΔG to equations 3 and 4 yield ΔC_p −1,115 ±18 cal mol^{-1} K^{-1}, T_H 298.6 ± 0.2 K and T_S 307.8 ± 0.1 K.

[b,c]Titrations of RPP29 into RPP21 at 20°C and 30°C were performed once and twice, respectively.

Table 2

Proton linkage revealed by the thermodynamics of titration of RPP29 into RPP21 in buffers with different ionization enthalpies, ΔH_{ion}, at pH 6.1 and pH 6.7, at 55°C.[a]

pH	Buffer	ΔH_{ion} [b] (kcal mol^{-1})	ΔH_{obs} (kcal/mol)	$\partial\Delta H_{obs}/\partial\Delta H_{ion}$
6.7	Cacodylate	−1.334	−32.0 ± 0.5	−0.7
	ACES	6.922	−37.6 ± 0.4	
6.1	Cacodylate	−1.344	−34.3 ± 0.1	−1.1
	ACES	6.922	−43.0 ± 0.2	

[a] Reported values are the average and standard deviation of three replicates at pH 6.7, and average and root mean square of the error of two replicates at pH 6.1.

[b] The buffer ionization enthalpy at 55°C are from published values of ΔH_{ion} and ΔC_P at 25°C. (26)